Geophys. J. Int. (2004) **157,** 838–852 doi: 10.1111/j.1365-246X.2004.02251.x

Interferometric/daylight seismic imaging

G. T. Schuster,[1] J. Yu,[1] J. Sheng[1] and J. Rickett[2]*

[1] *Geology and Geophysics Department, University of Utah, Salt Lake City, UT, USA. E-mail: schuster@mines.utah.edu*
[2] *ChevronTexaco Exploration and Production Technology Company,* 6001 *Bollinger Canyon Road, San Ramon, CA* 94583, *USA*

Accepted 2004 January 16. Received 2004 January 16; in original form 2003 May 5

SUMMARY

Claerbout's daylight imaging concept is generalized to a theory of interferometric seismic imaging (II). Interferometric seismic imaging is defined to be any algorithm that inverts correlated seismic data for the reflectivity or source distribution. As examples, we show that II can image reflectivity distributions by migrating ghost reflections in passive seismic data and generalizes the receiver-function imaging method used by seismologists. Interferometric seismic imaging can also migrate free-surface multiples in common depth point (CDP) data and image source distributions from passive seismic data. Both synthetic and field data examples are used to illustrate the different possibilities of II. The key advantage of II is that it can image source locations or reflectivity distributions from passive seismic data where the source position or wavelet is unknown. In some cases it can mitigate defocusing errors as a result of statics or an incorrect migration velocity. The main drawback with II is that severe migration artefacts can be created by partial focusing of virtual multiples.

Key words: interferometry, migration, reflectivity, seismic, stationary phase.

1 INTRODUCTION

Methods of passive seismic imaging can be divided into two categories: first, attempts to image the spatial locations of passive seismic sources themselves and, secondly, attempts to image the subsurface reflectivity that is illuminated by passive seismic energy.

1.1 Passive seismic source imaging

Passive seismic source imaging has the unique potential to provide direct measurements of subsurface permeability (e.g. Shapiro *et al.* 1999). Fluid flow causes fracturing; you image the fracturing; therefore, you are imaging the fluid flow. This, along with the growth of (both surface and borehole) time-lapse seismic, has led to the drive towards the electric oilfield, permanently instrumented and continually monitoring itself (Jack & Thomsen 1999).

To date, most of the published case studies of microseismic fracture imaging rely on earthquake-style hypocentral event triangulation. For example, Maxwell *et al.* (1998) describes the successful application of such technology to the Ekofisk field in the North sea.

1.2 Reflectivity imaging with passive seismic energy

Claerbout (1968) described the link between transmission and reflection seismograms via their autocorrelation functions for horizontally layered media. This may have inspired his conjecture that, by cross-correlating two passive traces, we can create the seismogram that would be computed at one of the locations if there was a source at the other.

Baskir & Weller (1975) describe possibly the first published attempt to verify this conjecture, by using passive seismic energy to image subsurface reflectivity. They briefly describe cross-correlating long seismic records to produce correlograms that could be processed, stacked and displayed as conventional seismic data. Unfortunately, their field tests seem to have been inconclusive.

Cole (1995) attempted to verify the conjecture with data collected using a 4000 channel 2-D field array on the Stanford University campus. Unfortunately, again, possibly as a result of the short (20 min) records or bad coupling between the geophones and the dry California soil, his results were inconclusive.

Following Cole's work, Rickett & Claerbout (1996) generated synthetic data with the phase-shift method. Their Earth reflectivity models consisted of (both flat and dipping) planar layers and point diffractors embedded in a $v(z)$ velocity function, and illuminated by random plane waves from below. They generated both pseudo-shot gathers (by cross-correlating one passive trace with many others nearby), and pseudo-zero-offset sections (by autocorrelating many traces). In these crosscorrelated domains, the kinematics for both point diffractors and planar reflectors, were identical to those predicted for real shot gathers and zero-offset sections. Rickett & Claerbout (1999) then experimented with moving the passive source location close to the receivers and reflectors, and included modeling with a $v(x, z)$ velolcity model. He observed that these changes did indeed affect the kinematics of the correlograms; however, changes

*Formerly of Geophysics Department, Stanford University, Palo Alto, CA, USA.

were small, and would probably not cause the method to fail in most situations.

The idea that a reflection seismogram could be created by cross-correlating two passive seismic records was rediscovered independently by the helioseismologists (Duvall *et al.* 1993), who created time–distance curves by cross-correlating passive solar dopplergrams recorded by the Michelson Doppler imager (Scherrer *et al.* 1995). Point-to-point traveltimes derived from these time–distance curves could then be used in a range of helioseismic applications (e.g. Giles *et al.* 1997; Kosovichev 1999). If helioseismic time–distance curves are averaged spatially, the result is equivalent to a multidimensional autocorrelation. Rickett & Claerbout (2000) demonstrated that multidimensional spectral factorization provides spatially averaged time–distance curves with more resolution than those calculated by autocorrelation. Their demonstration was restricted to layered models with no lateral velocity variation.

Katz (1990) received a patent for applying Claerbout's 1-D autocorrelogram imaging method to vertical seismic profile (VSP) data. Using VSP data obtained from a rotating drill bit, Katz (1990) showed that 1-D images of the reflectivity of the Earth could be obtained by autocorrelating the traces recorded on the free surface.

Daneshvar *et al.* (1995) autocorrelated seismograms from vertically incident microearthquakes recorded on the island of Hawaii. This generated pseudo-reflection seismograms, which showed reasonable agreement with a refraction study in the area. They followed a single channel approach and did not cross-correlate different channels.

Later, Schuster *et al.* (1997, 2003) and Yu *et al.* (2003) generalized the Katz (1990) algorithm from 1-D imaging to the theory of multidimensional migration of autocorrelograms.

Recently, Snieder *et al.* (2002) developed the theory of coda wave interferometry to determine the non-linear temperature dependence of the seismic velocity in granite. In this method, a seismogram recorded at an early time is cross-correlated with the seismogram recorded later in time when the temperature of the rock sample has changed. Temperature changes lead to mechanical changes in the rock, which amplify changes in the scattering coda.

1.3 Extending daylight imaging: interferometric imaging

Here we present the mathematical framework for imaging cross-correlated seismic data, i.e. interferometric imaging, for arbitrary reflectivity or source distributions. We show that interferometric imaging extends the daylight imaging concept to any number or distribution of sources and to arbitrary reflectivity distributions. Moreover, it offers new imaging opportunities, such as a very simple means to migrate multiples in data, migrate transmitted waves or locate unknown source locations from daylight data. Simply put, interferometric imaging can be described as cross-correlation migration (CCM) (Schuster 1999; Schuster & Rickett 2000) or an extended form of autocorrelation migration (Schuster *et al.* 1997).

Instead of exploiting the entire phase of arrivals, interferometric imaging exploits the phase difference between different arrivals. These phase differences can reveal subtle variations between the arrivals, which can be indicative of subtle changes in the medium properties. For example, sunlight on an oil slick at sea can produce a rainbow of interference patterns: reflections from the top of the oil slick interfere with those from its bottom to reinforce at certain light colors and thicknesses of the oil slick. The common ray path of the top and bottom reflections have equal and opposite phase that can cancel one another and the phase difference we see accounts for the phase change along the transit path in the oil. Similarly, seismologists can construct interferometric data by cross-correlating trace A with trace B. In this way we can exploit the phase difference between a certain arrival in trace A with certain arrivals in trace B. We will now generalize this interferometric imaging idea so that it extends the daylight imaging idea of Claerbout and his students to arbitrary reflectivity and source distributions. We also show how interferometric seismic imaging (II) can be used to image free-surface or peg-leg multiples from CDP data, generalize the receiver-function imaging of P-to-S (PS) transmitted waves used by seismologists and image the unknown location of buried sources.

Recently, Wapenaar *et al.* (2002) and Wapenaar *et al.* (2003) provided a special case of interferometric seismic imaging (II) based on seismic reciprocity. Wapenaar *et al.* (2003) extended Claerbout's autocorrelation theorem from a 1-D layered medium to an arbitrary inhomogeneous 3-D medium with randomly distributed sources below the irregular layers.

2 INTERFEROMETRY

For the last century, optical interferometry has played an extremely important role in advancing the fields of physics, astronomy and engineering. The key idea is that a light beam is used to sample the properties of an object or medium and is combined with a reference beam. The resulting interference pattern is sometimes called an interferogram and magnifies subtle optical properties of the object. Subtle changes are magnified because the interferogram highlights differences in the phases between the reference and sampling beams.

2.1 Optical interferometry

Fig. 1 depicts two interfering beams, where a laser beam illuminates the lower portion of the lens and the interferogram is recorded above the lens. The interferogram characterizes the interference between the reference direct wave (sA), denoted by

$$\tilde{d}_A = e^{i\omega\tau_{sA}}, \tag{1}$$

and the wave reflected within the lens (sArB) denoted by

$$\tilde{d}_B = R^2 e^{i\omega(\tau_{sA}+\tau_{Ar}+\tau_{rB})}. \tag{2}$$

Here, τ_{ij} is the propagation time along the path ij, R is the reflection coefficient associated with the glass-air interface and ω is the angular frequency of the optical wave. Dark lines in the interferogram denote the zones where the reflection and direct beams are out of phase and the in-phase zones depict coherent interference. An anomalous lens thickness will result in phase changes between the direct and reflected arrivals, so producing distortions in the ring-like features in the interferogram.

Mathematically, the interferogram is the intensity of the summed direct and reflected waves:

$$I = (\tilde{d}_A + \tilde{d}_B)(\tilde{d}_A + \tilde{d}_B)^* = 1 + 2R^2\cos[\omega(\tau_{Ar} + \tau_{rB})] + R^4, \tag{3}$$

where the intensity pattern I is controlled by the phase $\omega(\tau_{Ar} + \tau_{rB})$ along the reflected portion of the ray path. Note the important observation: the intensity or ring-like pattern is independent of the source phase or the position of the laser source along sA. This means that the source location or the source wavelet does not need to be known in order to delineate the lens geometry!

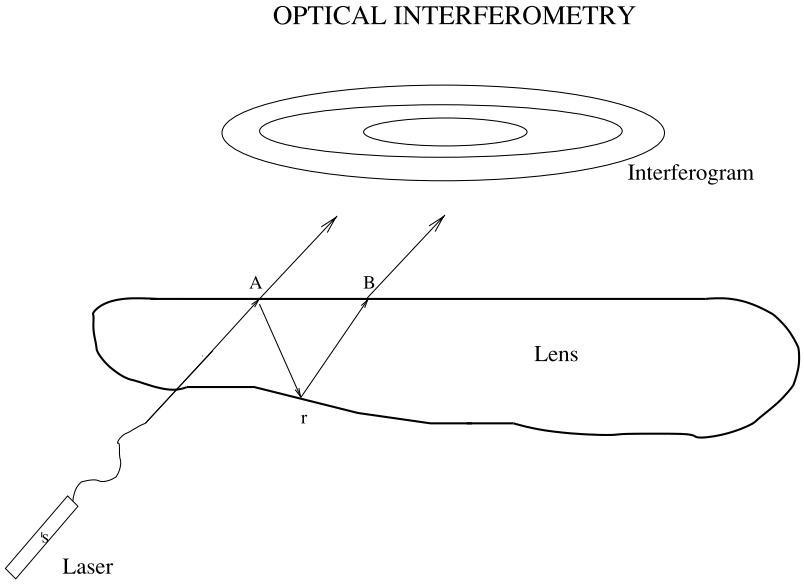

Figure 1. Interferogram produced by interference between direct arrivals (sA) and reflected arrivals (sArB) in the lens.

2.2 Seismic interferometry

Seismic interferometry is similar to optical interferometry, except seismic waves are used instead of an optical beam and the interferogram is obtained by cross-correlating neighbouring traces. As an example, Fig. 2(a) illustrates the case of a harmonic source at some unknown depth and with some unknown source wavelet. The goal is to estimate the reflectivity distribution from the seismic traces recorded at A and B (see eqs 1–2). Towards this goal we multiply the conjugate of the trace spectrum at A by the trace spectrum at B to give

$$\tilde{\Phi}_{AB} = \tilde{d}_A^* \cdot \tilde{d}_B = Re^{i\omega(\tau_{Ar}+\tau_{rB})} + o.t., \tag{4}$$

where $\tilde{\Phi}_{AB}$ denotes the product spectrum, the exponential term represents the correlation of the direct wave at A with the ghost reflection recorded at B, and $o.t.$ denotes other terms such as the direct–direct or reflected–reflected wave correlations. In this case, the direct arrival in trace A plays the role of the reference beam in optical interferometry, but in this paper we refer to trace A as the master trace.

Just like the laser intensity function in eq. (3), $\tilde{\Phi}_{AB}$ is a function of the phase $\omega(\tau_{Ar} + \tau_{rB})$ along the reflected portion of the ray path. Thus, changes in reflector geometry lead to changes in the correlated data $\tilde{\Phi}_{AB}$. Later, we will see how to recover the reflector geometry by applying the migration kernel $e^{-i\omega(\tau_{Ar'}+\tau_{r'B})}$ to $\tilde{\Phi}_{AB}$.

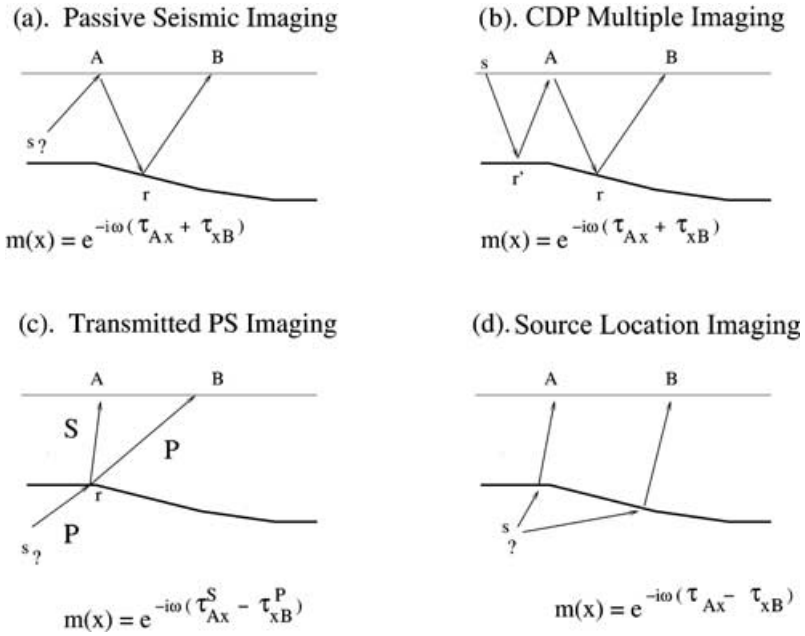

Figure 2. Cross-correlation migration kernels $m(x)|_{x=r}$ tuned to different correlated events for the data $\tilde{d}_A^* \tilde{d}_B$. (a) Buried source (such as a drill bit with unknown location) with the direct wave at A and the ghost reflection at B; (b) same as (a), except the source is at the surface and its location is known, such as in CDP data; (c) correlated event is the transmitted P wave at B and the transmitted PS wave at A; (d) same as (c), except now the source location is sought and the two correlated events are the direct P waves at A and B.

The key problem with seismic interferometry is that other events in trace A, such as reflections, can act as false reference beams. These false reference beams appear in the o.t. in eq. (4) and can give rise to unwanted artefacts in the migration image. A possible remedy is to purify trace A by windowing out all but the direct arrival (see Sheley & Schuster 2003), but this is only practical for, typically, non-passive data.

3 INTERFEROMETRIC SEISMIC IMAGING

Interpretation of the raw interferograms in eq. (4) for subsurface geology is too cumbersome. Instead, an image of the reflectivity distribution can be obtained by migrating the cross-correlated traces, otherwise known as II (Schuster 2001). Cross-correlation migration is similar to standard migration in that an imaging condition is applied to the back-projected data, except in seismic interferometry the input data are the crosscorrelograms. Several examples of II will now be presented: imaging of the reflectivity distribution from data generated by sources below and on the free surface, and imaging of buried source locations.

3.1 Ghost reflection cross-correlogram imaging with buried sources

Fig. 2(a) illustrates the case where a drill bit at depth radiates seismic energy that is recorded on the free surface. The source wavelet in the frequency domain is denoted as $\tilde{W}_i(\omega)$, where i denotes the ith source wavelet to account for the fact that the drill bit can occupy widely separated positions in depth, each characterized by a different wavelet. The phase of the source wavelet at the ith position is random and assumed to be uncorrelated with the source wavelet at other positions, i.e. $w_i(t) \otimes w_j(t) = 0$ for $i \neq j$. Unless otherwise indicated, an acoustic medium is assumed and the data at the free surface are the measured pressure fields of upgoing waves.

The goal is to use ghost reflections to reveal the geological layering, despite the fact that the bit location is uncertain and the source wavelet is very ringy. This is a problem that can be solved by II: cross-correlation tends to collapse ringy source wavelets to short duration and also eliminates the need to know the source location, as shown in the following steps.

(i) The frequency-domain traces at positions B and A are given by (see Fig. 2a)

$$\begin{aligned}\tilde{d}_B &= \tilde{W}_i(\omega)e^{i\omega\tau_{sB}} - \tilde{W}_i(\omega)Re^{i\omega(\tau_{sA}+\tau_{Ar}+\tau_{rB})} + o.t.,\\ \tilde{d}_A &= \tilde{W}_i(\omega)e^{i\omega\tau_{sA}} - \tilde{W}_i(\omega)Re^{i\omega(\tau_{sA'}+\tau_{A'r'}+\tau_{r'A})} + o.t.,\end{aligned} \tag{5}$$

where the specular-ghost and direct-wave terms are explicitly written, while *o.t.* represents the other terms such as primary reflections, multiples and diffractions. Geometrical spreading is harmlessly ignored and the angle-dependent reflection coefficient at the layer interface is approximated as the constant R. The ray $sArB$ is the specular ray path for the free-surface ghost reflection that begins at s and terminates at B as shown in Fig. 2(a). Similarly, $sA'r'A$ is the associated ray path for the specular ghost reflection that also begins at s but terminates at A. Here, A' is the specular reflection location (not shown) at the free surface.

(ii) Form the correlated data. Cross-correlating trace A with trace B gives

$$\begin{aligned}\tilde{\Phi}(A,B) &= \tilde{d}_A^* \cdot \tilde{d}_B\\ &= |\tilde{W}_i(\omega)|^2[e^{i\omega(\tau_{sB}-\tau_{sA})} \quad (\mathrm{dir}_A\text{–}\mathrm{dir}_B)\\ &\quad - R(e^{i\omega(\tau_{Ar}+\tau_{rB}+\tau_{sA}-\tau_{sA})} \quad (\mathrm{dir}_A\text{–}\mathrm{gh}_B)\\ &\quad + e^{i\omega(\tau_{sB}-\tau_{sA'}-\tau_{A'r'}-\tau_{r'A})}) \quad (\mathrm{dir}_B\text{–}\mathrm{gh}_A)\\ &\quad + R^2e^{i\omega(\sum\tau)}] + \ldots\ldots, \quad \mathrm{gh}_B - \mathrm{gh}_A\\ &= -|\tilde{W}_i(\omega)|^2Re^{i\omega(\tau_{Ar}+\tau_{rB})} + o.t.,\end{aligned} \tag{6}$$

where $\sum\tau = -\tau_{sA'} - \tau_{A'r'} - \tau_{r'A} + \tau_{sA} + \tau_{Ar} + \tau_{rB}$, dir is direct and gh is ghost. The dir_A–gh_B correlation is of the most importance because it does not contain the unknown source-phase term $\omega\tau_{sA}$. In fact, $\tilde{\Phi}(A,B) \approx -Re^{i\omega(\tau_{Ar}+\tau_{rB})}$ is kinematically equivalent to a shot gather of primary reflections with a source at A and traces at B.

(iii) Migrate the dir_A–gh_B correlations in $\tilde{\Phi}(A,B)$. The migration kernel should be tuned to annihilate the phase of the gh_B–dir_A correlation when the trial image point is at the reflector. This is accomplished by multiplying $\tilde{\Phi}(A,B)$ by the ghost migration kernel

$$e^{-i\omega(\tau_{Ax}+\tau_{xB})} \tag{7}$$

and summing over all frequencies, virtual source (i.e., master trace) positions A and geophones B to yield the migration image $m(x)$ at x:

$$\begin{aligned}m(x) &= \sum_\omega\sum_{A,B}\tilde{\Phi}(A,B)e^{-i\omega(\tau_{Ax}+\tau_{xB})},\\ &= \sum_{A,B}\phi(A,B,\tau_{Ax}+\tau_{xB}),\end{aligned} \tag{8}$$

where $\phi(A,B,t)$ is the temporal correlation between the traces at A and B with lag time t. When x is coincident with the actual specular reflection point at r, then there will be annihilation of the dir_A–gh_B phase $\omega(\tau_{Ar}+\tau_{rB})$ in eq. (6) to give maximum migration amplitude for $x \to r$ for all ω. The o.t. will, hopefully, be incoherently focused just like the migration of actual multiples by Kirchhoff migration (KM). The surprise is that the ghost reflection can be used to image the reflector even though we do not know the source location or the source time history! The above equation is that of standard pre-stack diffraction-stack migration, except the input data are the cross-correlograms, the summation over A is over the virtual source positions and the B summation is over the traces in each virtual shot gather.

The above methodology is applicable to any number of sources, any depth of source burial and can approximately image an arbitrary reflectivity distribution. For multiple sources contemporaneously excited, the success of this method demands that the source wavelet time histories be uncorrelated, e.g. a random time-series.

One of the implicit assumptions is that the trace at A is at the specular reflection point on the free surface for the $sArB$ ray path. For a high-frequency source at s, non-specular reflections from the free surface do not significantly contribute to the imaging at r as shown by stationary-phase analysis in the Appendix. Also, practical implementation of this procedure requires a double-time derivative of the data (Schuster *et al.* 2003).

3.1.1 *Five-layer synthetic data example.*

A five-layer geological model was used to test the cross-correlogram migration method and roughly represents the recording geometry and model for drill-bit data collected in a W. Texas experiment (see Yu *et al.* 2003). The top panel in Fig. 3 shows the velocity model used for cross-correlogram migration. The synthetic drill-bit source moved horizontally at a depth of 1500 m and the drill bit moved in the horizontal direction from 1650 to 1940 m during the recording sessions. The data were recorded with a source interval of 5 m. The

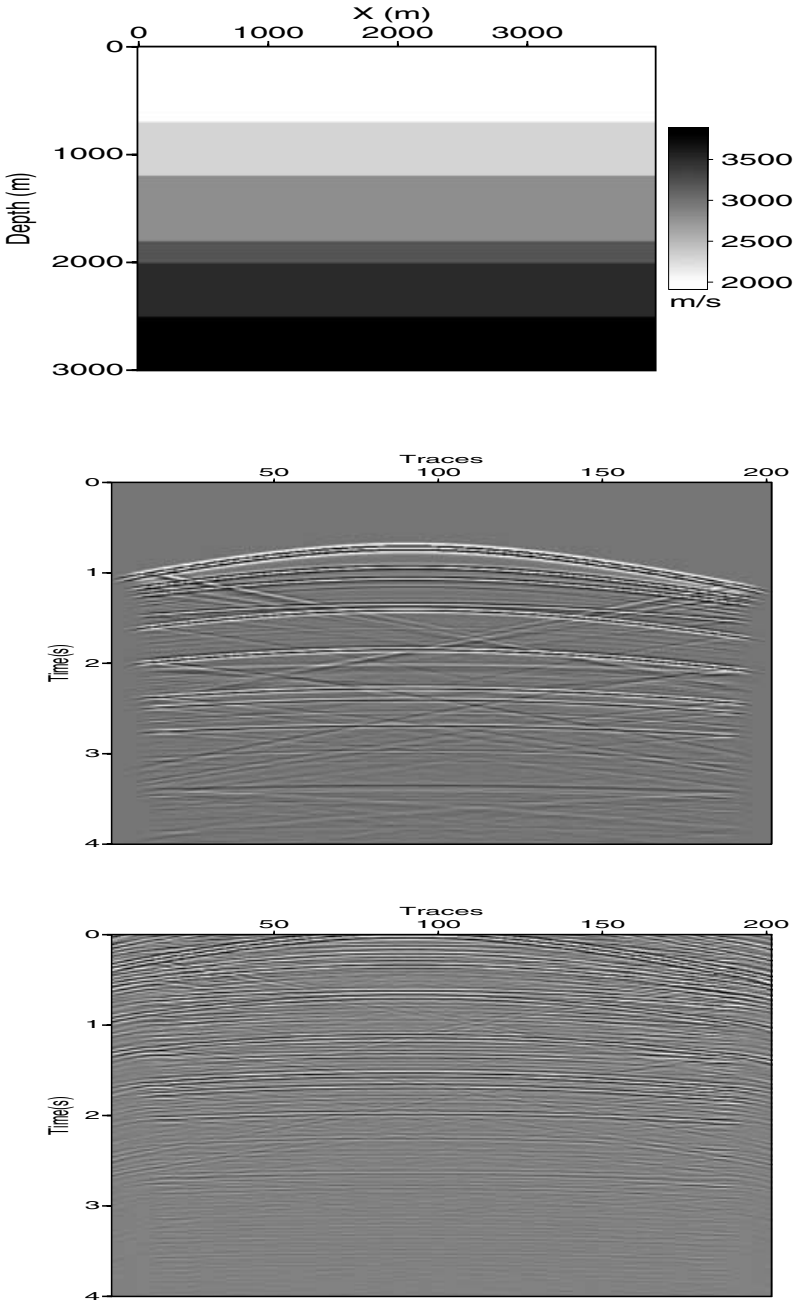

Figure 3. (Top) Velocity model, (middle) shot gather for a buried source and (bottom) cross-correlograms using trace 80 as the master trace.

receivers were evenly deployed on the surface over a lateral range of 4000 m and the receiver interval was 20 m; there were a total of 39 common source gathers (CSG) recorded. The synthetic data were generated by a finite-difference solution to the acoustic wave equation.

The middle panel in Fig. 3 shows a typical common source gather. Besides primary reflections, there are free-surface related ghost reflections and interbed multiples. The bottom panel in Fig. 3 shows the cross-correlograms computed from the middle panel shot gather.

Applying eq. (8) to the time derivative of these data gives the migration images shown in Fig. 4. The top panel shows that the cross-correlogram migration image has spurious events caused by partial focusing of virtual multiples such as direct–primary correlations. Using velocity filtering to separate the primary reflections in the input data, the false reflectors have mostly disappeared and the subsurface structure is well reconstructed as shown in Fig. 4.

3.2 Ghost reflection autocorrelogram imaging with buried sources

We will now assume that the source position at depth is known, which will allow us to reduce computational expense by only having to migrate autocorrelograms. In addition, migration of autocorrelograms significantly reduces the defocusing as a result of both migration velocity errors and static effects (Sheley & Schuster 2003; Yu *et al.* 2003).

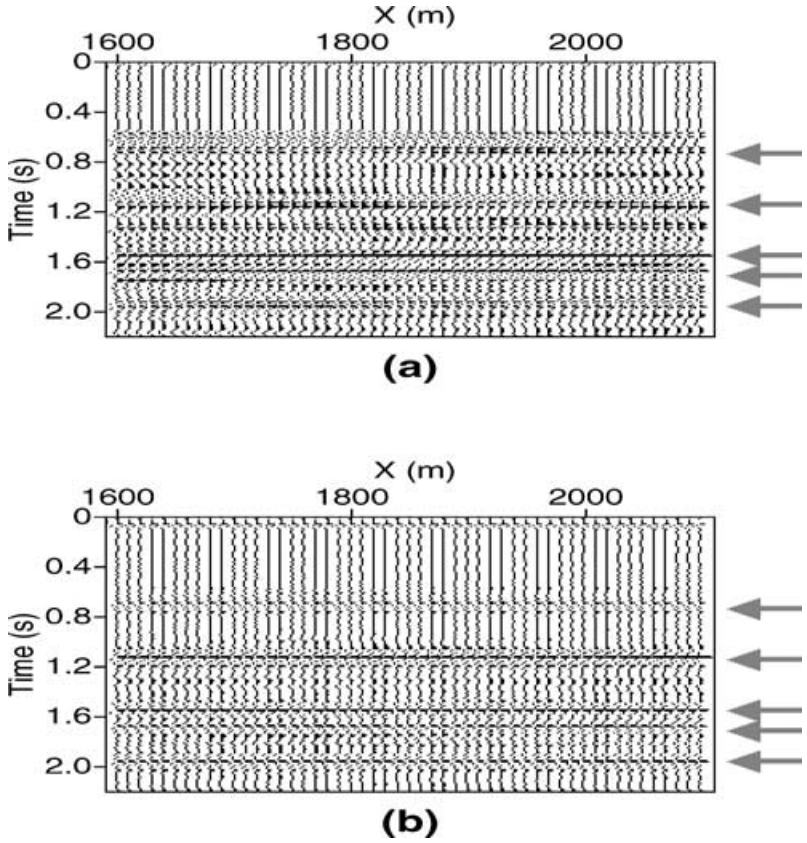

Figure 4. Cross-correlogram migration images in time domain: (a) with primary and ghost reflections and (b) without primary reflections. Here the migration operator is tuned to the correlation between the direct wave and the ghost reflection. The arrows indicate the actual reflector locations.

To understand these last statements, include the specular primary reflection term in eq. (5) so that

$$\tilde{d}_B = \tilde{W}_i(\omega)\left[e^{i\omega\tau_{sB}} + Re^{i\omega(\tau_{sr'}+\tau_{r'B})} - Re^{i\omega(\tau_{sA}+\tau_{Ar}+\tau_{rB})}\right] + \cdots. \tag{9}$$

where r' and r are the specular reflection points at the layer interface for the $sr'B$ and $sArB$ rays, respectively. The autocorrelation function for the trace at B becomes

$$\begin{aligned}\tilde{\Phi}(B, B) = |\tilde{W}_i(\omega)|^2[1 + 2R^2 \\ + 2R(\cos\omega(\tau_{sB} - \tau_{sr'} - \tau_{r'B}) \quad (\text{prim}_B\text{–dir}_B) \\ - \cos\omega(\tau_{sB} - \tau_{sA} - \tau_{Ar} - \tau_{rB}))] + o.t \quad (\text{gh}_B\text{–dir}_B),\end{aligned} \tag{10}$$

where prim is primary.

If the source position at s and the migration velocity are known, then the rays for the ghost reflections can easily be computed to give the traveltime fields $\tau_{sA'} + \tau_{A'x}$ for all subsurface points x and their specular free-surface reflection points A'. Note, A' depends on the source point location and the trial image point location x.

The migration kernel $e^{-i\omega(\tau_{sB}-\tau_{sx}-\tau_{xB})}$ focuses $\text{prim}_B - \text{dir}_B$ correlations to the layer interface. The resulting migration image will be denoted as the primary autocorrelation image $m(x)_{\text{prim}}$:

$$\begin{aligned}m(x)_{\text{prim}} &= \sum_{\omega}\sum_{B} e^{-i\omega(\tau_{sB}-\tau_{sx}-\tau_{xB})}\tilde{\Phi}(B, B), \\ &= \sum_{B}\phi(B, B, \tau_{sB} - \tau_{sx} - \tau_{xB}).\end{aligned} \tag{11}$$

In addition, the gh_B–dir_B correlations can be focused to the layer interface by applying the migration kernel $e^{-i\omega(\tau_{sB}-\tau_{sA}-\tau_{Ax}-\tau_{xB})}$ to yield the ghost autocorrelation image.

$$\begin{aligned}m(x)_{\text{ghost}} &= \sum_{\omega}\sum_{B} e^{-i\omega(\tau_{sB}-\tau_{sA}-\tau_{Ax}-\tau_{xB})}\tilde{\Phi}(B, B), \\ &= \sum_{B}\phi(B, B, \tau_{sB} - \tau_{sA} - \tau_{Ax} - \tau_{xB}).\end{aligned} \tag{12}$$

An advantage of knowing the source location is that the autocorrelation migration equation needs to sum only once over the geophone positions compared to the double nested loop over geophone positions in the CCM in eq. (8). This results in less computation time and fewer migration artefacts. The additional loop over geophone index A in eq. (8) is needed in order to involve the trace at the unknown specular reflection location on the free surface (see Fig. 2a). Location A is unknown for a source buried at an unknown location.

Fig. 5 depicts the ghost and joint autocorrelation migration images for the five-layer model. The joint image was obtained by computing the joint product of $m(x)_{\text{gh}}$ and $m(x)_{\text{prim}}$. Note, the joint image is almost free of migration artefacts.

3.2.1 W Texas drill-bit data.

Drill-bit seismic data were recorded with ten three-component receivers in W. Texas by Union Pacific Resources Co. (UPRC); the receivers were equi-spaced between 822 and 2100 m from the drill rig as shown in Fig. 6. The data were recorded on the free surface of the Earth while a tri-cone drill-bit and down-hole motor were used to drill along a horizontal trajectory at a depth of 2800 m in the Austin Chalk formation. There were approximately 609 shot gathers, each

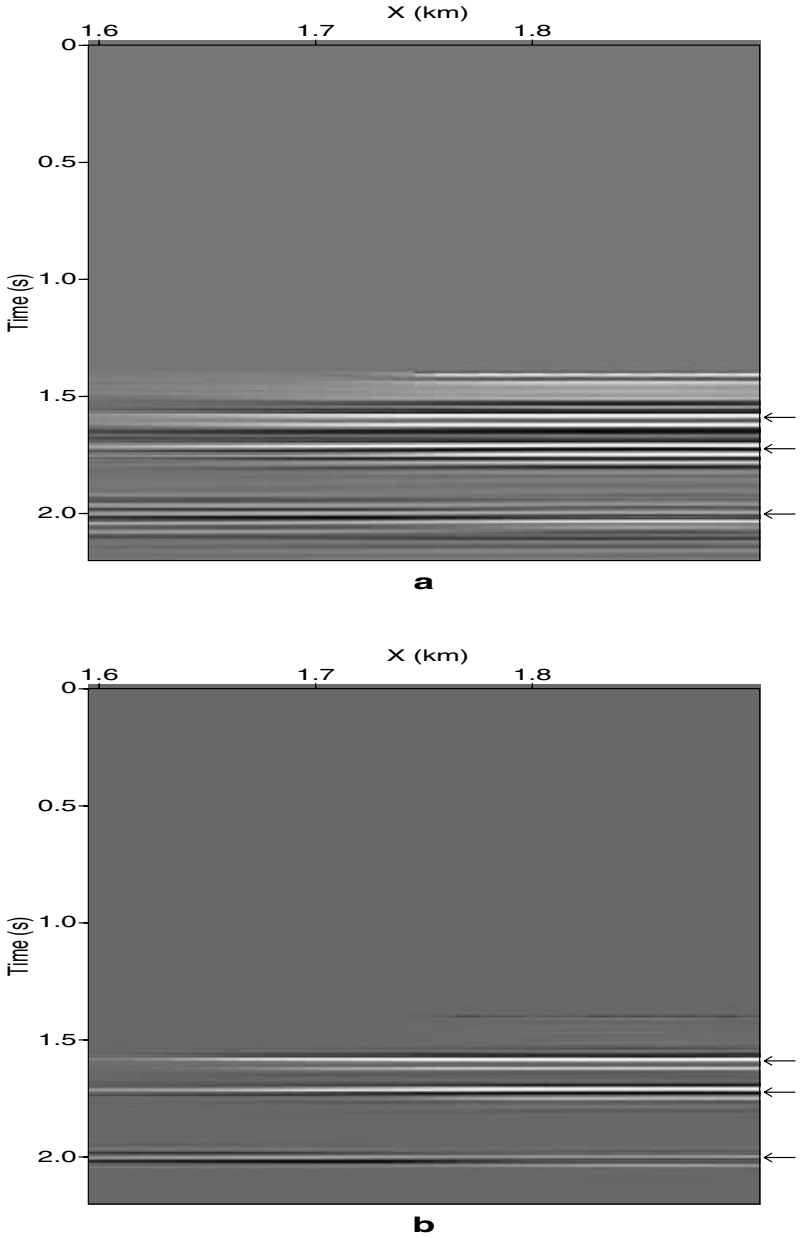

Figure 5. (Top) Ghost autocorrelation migration image and (bottom) joint image using both the primary and ghost autocorrelation images for the five-layer model.

with a recording length of approximately 20 s with a sample interval of 2 ms. Because the seismic data were distorted by strong noise, the data were pre-processed as described by Yu *et al.* (2003).

The inset in the bottom panel of Fig. 7 shows the joint autocorrelogram migration result using both primary and ghost reflections, where the trace interval is approximately 3.038 m. The top panel shows the primary autocorrelation migration image. In comparison, it can be seen that joint autocorrelogram migration generates a look-ahead image with less interference.

3.3 Free-surface multiple imaging with CDP data

Now we will show how interferometeric imaging can be used to migrate first-order free-surface multiples in CDP data. In comparison to the Delft method (Berkhout & Verschuur 1998, 2000) of autoconvolving traces and subtracting the computed multiples from the original traces, we will cross-correlate the data to generate shifted multiples kinematically equivalent to primaries and migrate these multiples. The multiple migration image is then combined with the primary reflection migration section to determine the common reflector locations. Delft's strategy to attack interbed multiples can be followed as well, except with interferometry the interbed multiples are incorporated into the migration section.

Placing the source at the surface gives rise to the diagram in Fig. 2(b). Here the first-order free-surface multiple recorded at B and the primary reflection recorded at A are explicitly represented by

$$\tilde{d}_B = R^2 \tilde{W}(\omega) e^{i\omega(\tau_{sr'}+\tau_{r'A}+\tau_{Ar}+\tau_{rB})} + o.t., \tag{13}$$

$$\tilde{d}_A = -R \tilde{W}(\omega) e^{i\omega(\tau_{sr'}+\tau_{r'A})} + o.t., \tag{14}$$

where only the terms of interest are explicitly included in the equation. The cross-correlation of these two traces annihilates the

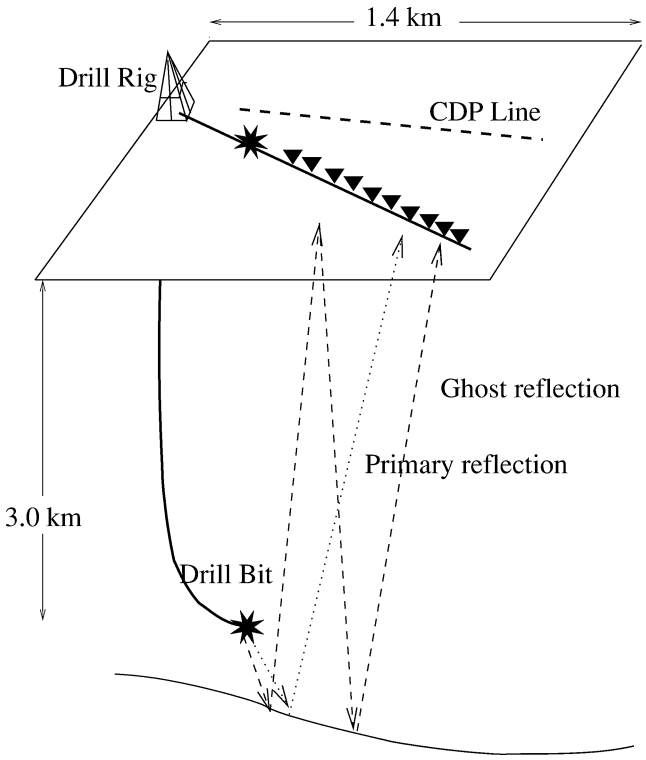

Figure 6. W Texas dill rig and seismic recording configuration, where the drill bit acts as a seismic source wavelet with random phase.

common phase terms in the exponents to give

$$\tilde{d}_A^* \cdot \tilde{d}_B = -R^3 |\tilde{W}(\omega)|^2 e^{i\omega(\tau_{Ar}+\tau_{rB})} + \cdots, \tag{15}$$

where the phase term in this equation suggest kinematics equivalent to a primary reflection generated by a source at A and a receiver at B. This is similar to the case of a buried source except the strength of the correlation has been reduced in eq. (6) from R to R^3!

The obvious migration kernel for the correlated data is given by $e^{-i\omega(\tau_{Ax}+\tau_{xB})}$, so the migration equation is exactly the same as eq. (8). However, a major problem is that the migration kernel is tuned to a correlation with a weak strength of R^3. This weak correlation competes with stronger correlations, such as primary with primary correlations that are R^2 strength that can inadvertently be tuned to the multiple migration kernel.

Notice that the location A for the trace $\tilde{d}_A$ in eq. (14) was judiciously selected at the specular bounce point of the ghost at the free surface. However, the specular bounce point A is not known, so how can this be done? The trick is to apply the migration kernel to the correlated data $\tilde{d}_A^* \tilde{d}_B$ and sum over all trace positions A in the shot gather:

$$m(x) = \sum_{\omega} \sum_{A'} \tilde{d}_{A'}^* \cdot \tilde{d}_B e^{-i\omega(\tau_{A'x}+\tau_{xB})}. \tag{16}$$

Stationary phase theory (see Appendix) says that the asymptotic dominant contribution to the migration image occurs under two conditions: (i) the trial image point x coincides with the actual specular reflection point r on the layer interface, and (ii) the summation index A' coincides with the specular bounce point A of the ghost on the free surface. Otherwise, the contributions from the eq. (16) summation in A' are negligible for high frequencies.

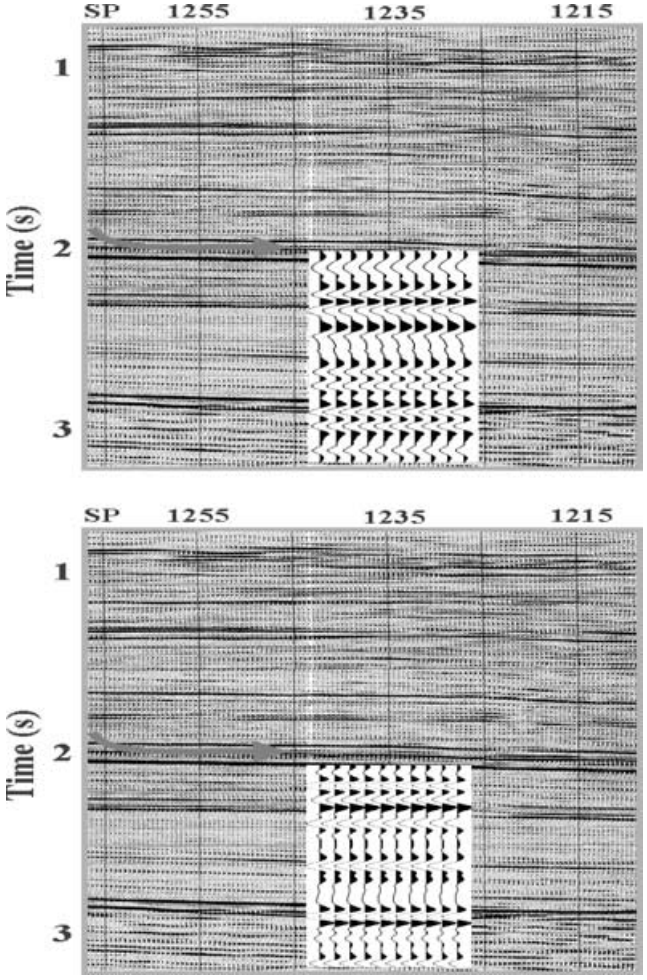

Figure 7. (Top) Ghost autocorrelation migration image and (bottom) joint image using both the primary and ghost autocorrelation images for the W Texas data.

3.3.1 SEG/EAGE salt model data.

The SEG/EAGE salt model is chosen to test the effectiveness of migrating multiples in CDP data (Sheng 2001). The top illustration in Fig. 8 shows profile *A–A* from the SEG/EAEG salt model. The model used is 17 120 m by 4000 m, with a trace interval of 27 m and a trace recording length of 5 s. There are 320 shot gathers, each with 176 traces. The middle and bottom images show the pre-stack Kirchhoff and cross-correlogram migration images, respectively. As expected, the cross-correlation images contain more artefacts because the virtual multiples are migrated to incorrect locations. Similarly, but not to the same severity, the Kirchhoff image also contains incorrectly imaged multiples. The arrows in the Kirchhoff image point towards the incorrect imaging of multiples.

Both the cross-correlation and Kirchhoff images show the events correctly imaged at the actual reflector positions, but the cross-correlation image is severely polluted by artefacts. Therefore, a weight w_i can be computed that grades the similarity between the Kirchhoff $KM(i)$ and cross-correlation $CCM(i)$ images in a local window centered at the ith pixel. The weight w_i is computed by correlating the KM traces with the corresponding CCM traces in a small window for each migrated shot gather. In practice, the window is 40 traces wide and 20 sample points tall. The final merged image

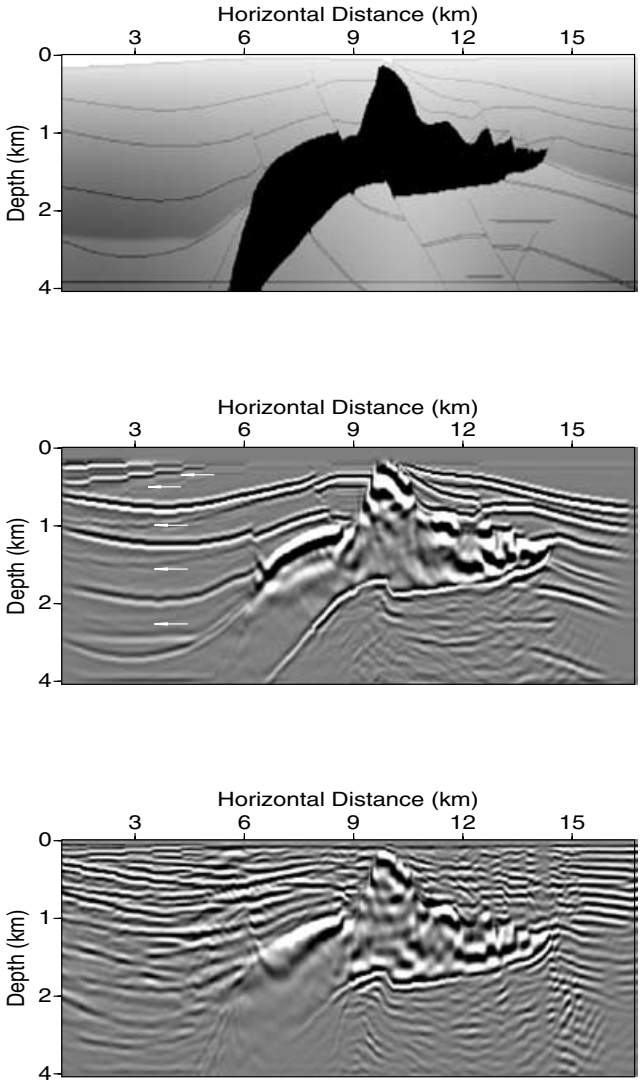

Figure 8. (Top) SEG/EAGE salt model, (middle) Kirchhoff pre-stack migration image, (bottom) cross-correlation migration image.

for a migrated shot gather can be obtained by

$$\text{Merged}(i) = w_i K M(i) \tag{17}$$

and the composite merged imaged is computed by summing the merged images for all shot gathers.

The merged image obtained by applying the above procedure to the CCM and KM images is given in Fig. 9. It can be seen that at the left part of the image the true reflectors are enhanced and the artefacts caused by the free-surface multiples are attenuated. Below the salt body, it does not show much improvement which might be the result of the KM method itself.

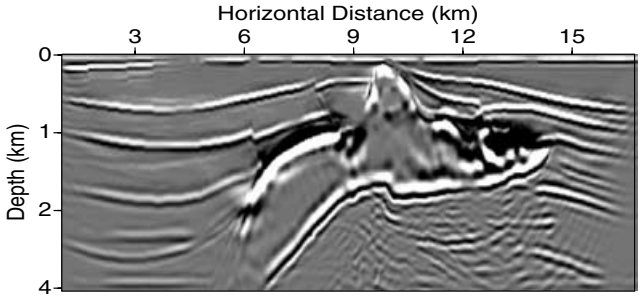

Figure 9. Blended image of Kirchhoff and cross-correlation migration images.

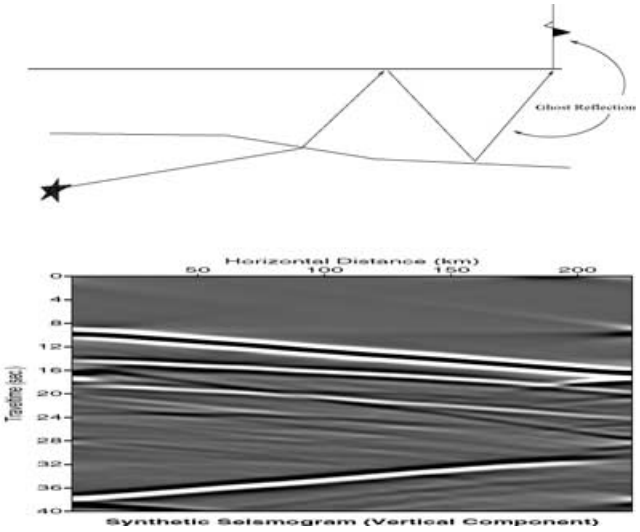

Figure 10. (Top) Ray diagram for an earthquake generating a ghost reflection from the free surface, (bottom) vertical-component seismograms (particle velocity) generated by a teleseismic plane *P* wave with an incident angle of 10°. The direct and ghost reflections are prominent where the crustal model is the four-layer crustal model for Utah.

3.4 Teleseismic receiver function imaging

Seismologists use converted PS transmission waves to image the geometry of a layer interface, often the Moho (Langston 1977; Bostock & Rondenay 1999; Sheley & Schuster 2003). For a recorded teleseismogram, they cross-correlate the vertical component with the horizontal component, where the largest correlation amplitude is presumed to be the converted PS transmitted wave at the Moho. The lag time of this PS correlation is related to the depth of the Moho if the P/S velocity ratio is known. Fig. 2(c) shows the ray diagram for transmitted waves that are converted at the interface. It can be seen from this diagram that the cross-correlation of trace *A* with *B* will annihilate the common phase term along the ray *sr*, so that the PS transmission migration kernel is shown in the figure.

As an example of imaging the crust with teleseismic ghost reflections (Sheng *et al.* 2001), elastic seismograms from a plane *P*-wave source were computed by a 2-D finite-difference solution to the elastic wave equation. Fig. 10 shows these seismograms with a source incidence angle of 10°. Direct and surface reflected phases are seen in the data where the crustal model is a four-layer model shown by the white lines in Fig. 11. The model is modified from an E–W cross-section across northern Utah by Loeb & Pechmann (1986); the trough in the third layer boundary was added for testing purposes. The source time history was modelled as a Ricker wavelet with a peak frequency of 0.6 Hz and a bandwidth of approximately 0.2 to 1.2 Hz. The station spacing is 1 km.

Fig. 11 shows the reflector image of the four-layer crustal model obtained by migrating ghost reflections (eq. 8) in the synthetic teleseismic record. The result of the correlogram migration is that the upper two interfaces are correctly imaged, while the third one is contaminated by a second-order ghost. It is expected that data from different incidence angles will suppress this source of coherent noise.

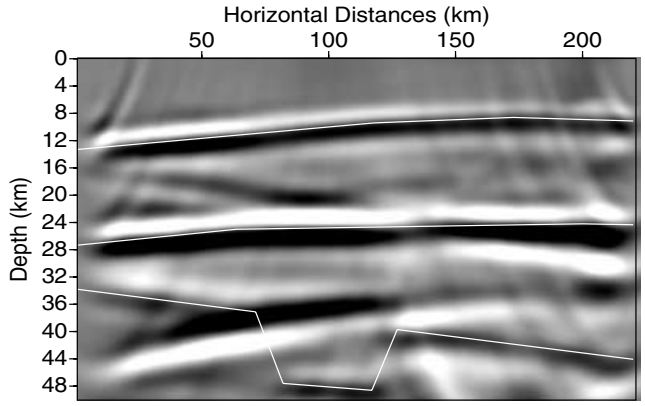

Figure 11. Image of interfaces after cross-correlogram migration of the surface reflected *P* waves in the cross-correlated data in the previous figure. The first and second interfaces (white solid lines) are correctly imaged, but the deepest interface is obscured by spurious events in the correlated records that could be reduced by stacking more teleseismic records. Interface model (white lines) is similar to that of the crust along an east–west profile in central Utah.

3.5 Source location imaging

Sometimes it is desirable to locate the unknown position of a seismic source, such as in the case of a hydro-frac test where the induced fracture location indicates the fluid pathway. In this case, we can use the dir_A–dir_B correlation in eq. (6) to find the unknown source position s in Fig. 2(d). That is, apply the migration kernel $e^{-i\omega(\tau_{xB}-\tau_{xA})}$ to the data $\tilde{\Phi}(A, B)$ to get the migration image of the source locations:

$$m(x) = \sum_{A,B}\sum_{\omega} \tilde{\Phi}(A, B)e^{-i\omega(\tau_{xB}-\tau_{xA})}, \\ = \sum_{A,B} \phi(A, B, \tau_{xB} - \tau_{xA}). \tag{18}$$

Single scattering synthetic data generated by a ray tracing method will be used to test this concept.

Fig. 12(a) shows synthetic data generated for a point source centered 1050 m below a 2100 m wide array. There are 70 geophones in the array with a geophone spacing of 30 m. The traces are computed for duration of 1 s with a 30 Hz Ricker wavelet source. The point scatterer responses of the diffraction stack migration and the CCM are shown in Figs 12(b) and (c), respectively. Note, the cross-correlation image of the point scatterer is smeared over a larger depth range than that of the Kirchhoff image. This is because the cross-correlation of one trace with another smears the source wavelet into a longer wavelet and also because the cross-correlation migration kernel has poor resolution in the depth direction. Nevertheless, the cross-correlation point-scatterer image is acceptable.

In practice, the trace at the master trace location and its two nearest neighbours were muted because the direct wave migration kernel in eq. (18) has zero or nearly zero phase when $A \approx B$. This is undesirable because any energy from these traces will be smeared uniformly throughout the model, not just at the buried source points. Also, a second derivative in time was applied to the cross-correlogram traces.

Fig. 13 is the same as Fig. 12 except the source wavelet is a long random time-series. The cross-correlation of traces collapses the ringy time-series to an impulse-like wavelet so that the associated

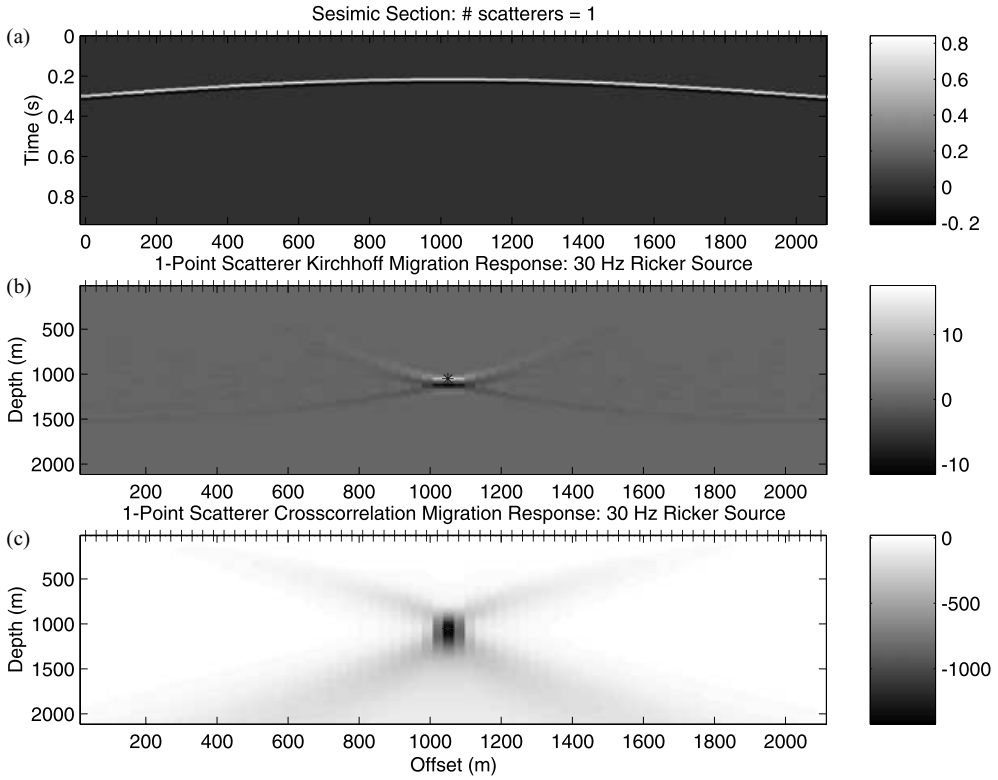

Figure 12. (Top) Synthetic 30 Hz data generated by an impulsive like point source (*) at a depth of 1050 m. The point source exploded at time zero. (Middle) Kirchhoff migration image. (Bottom) Cross-correlation migration image. The Kirchhoff image is better resolved partly because temporal cross-correlation of traces will broaden the wavelet.

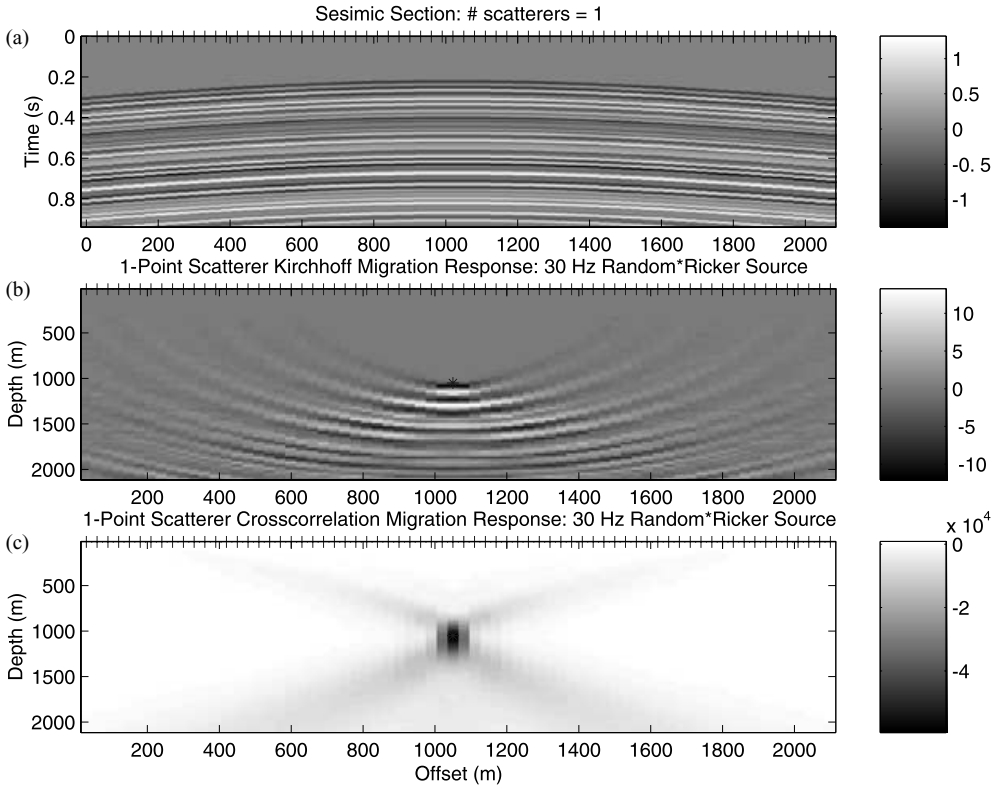

Figure 13. Same as Fig. 12, except a long random time-series is used for the source wavelet that is excited at time zero. Note, that the cross-correlation of traces collapses the ring-like source wavelet into an impulsive-like wavelet, leading to a better resolved migration image in the cross-correlogram image.

migration image in Fig. 13(c) has good spatial resolution compared with the Kirchhoff image in Fig. 13(b).

In the previous examples, the scatterer exploded at time zero. Now, there are ten scatterers and all are assumed to explode at random times with a random time-series as a source wavelet. The resulting data for 1 s is shown in Fig. 14(a). Fig. 14(b) shows these data after a CCM of 1 s of data and roughly locates the position of the 10 point sources. Repeating this CCM for fifteen data sets, each with 1 s of data generated from ten point scatterers with distinct random time histories, yields the stacked images in Fig. 14(c). As expected, averaging the migration images tends to cancel migration noise and reinforce the energy at the location of the point sources.

Finally, the fault-like structure denoted by stars in Fig. 15 is assumed to emanate seismic energy randomly in time with random strength. This might approximate the situation where fluid is injected along a reservoir bed and seismic instruments are passively monitoring the location of the injection front. Fig. 15 shows the results after CCM of (middle) 1 s of data and (bottom) 40 stacks of 1 s records. The fault boundaries are much better delineated in the 40-stack migration image, although the resolution is much worse than that of an ordinary seismic survey.

Poor resolution of the cross-correlation images is consistent with the poor vertical resolution predicted by the CCM impulse response shown in Fig. 16. Note that the traveltime difference $\tau_{xB} - \tau_{xA}$ is the same for a scatterer buried at any depth midway between the source and receiver. Thus, the vertical resolution is very poor for a midpoint image estimated from this trace.

A possibility for improving resolution is to measure the incidence angle of energy in the cross-correlograms and use this angle as a constraint in smearing data into the model. This strategy is similar to that of ray-map or wave-path migration (Sun & Schuster 2001), but it remains to be seen if this is a practical strategy with cross-correlograms.

4 MODEL RESOLUTION

The asymptotic theory of Beylkin (1985) predicts that the wavenumber **k** of the model spectrum estimated from primary reflection data is given by

$$\mathbf{k} = \omega(\nabla\tau_{Ax} + \nabla\tau_{Bx}), \tag{19}$$

where A and B denote the source and trace positions, respectively, and x denotes the location of the estimated reflectivity model. In a homogeneous medium, the vertical wavenumber of the reflectivity model estimated from a zero-offset trace directly above x is $\mathbf{k} = \omega(\nabla\tau_{Ax} + \nabla\tau_{Bx}) = 2\omega/c\hat{\mathbf{k}}$, where c is the velocity and $\hat{\mathbf{k}}$ is the unit vector in the vertical direction. This implies that the vertical resolution is half the wavelength, as expected. Eq. (19) is also valid for the II of multiples described in this paper when the selected cross-correlation data are kinematically equivalent to primary reflections, e.g. eq. (8).

However, the model wavenumber estimated from the source location imaging described by eq. (18) is given as

$$\mathbf{k} = \omega(\nabla\tau_{Bx} - \nabla\tau_{Ax}), \tag{20}$$

where A and B represent the locations of the two geophones. In this equation, the sign in front of $\nabla\tau_{Ax}$ is negative because the energy from the scatterer propagates upward to both A and B. Compare this to eq. (19) for primary reflection data where the energy propagates down from the source at A to the scatterer and back up to the geophone at B. If the scatterer is located midway at depth z between the two geophones then eq. (20) becomes $\mathbf{k} = \omega(\nabla\tau_{Bx} - \nabla\tau_{Ax}) =$

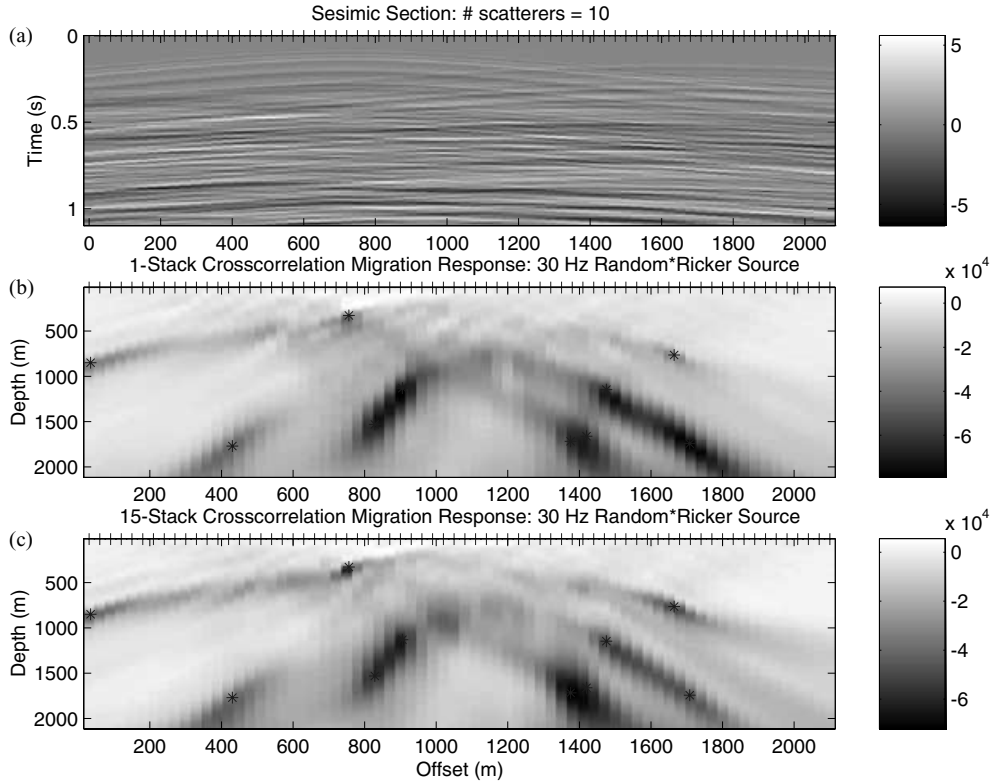

Figure 14. Similar to Fig. A13, except the source wavelets of 10 point sources (*) are generated by a random number generator. The middle image shows the cross-correlogram image computed from 1 s of data, while the bottom images shows the result after 15 stacks of 1-s data. The stacked image is better resolved because stacking tends to cancel noise and reinforce migration energy at the point source locations.

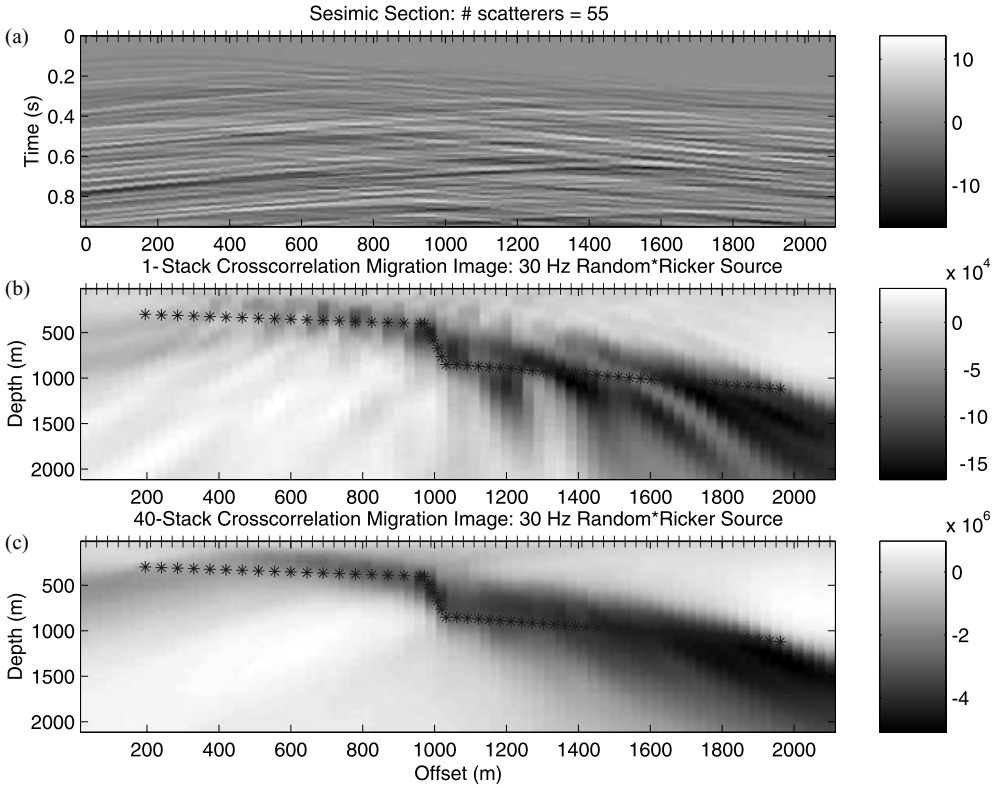

Figure 15. (Top) Synthetic 30 Hz data generated by 55 point source located along a fault-like boundary. The points exploded at random times with random weighting amplitudes. (Middle) Cross-correlation migration image obtained from 1 s of data. (Bottom) Cross-correlation migration image after 40 stacks of 1-s data. The stacked image appears to be less noisy and a better approximation to the fault geometry delineated by stars.

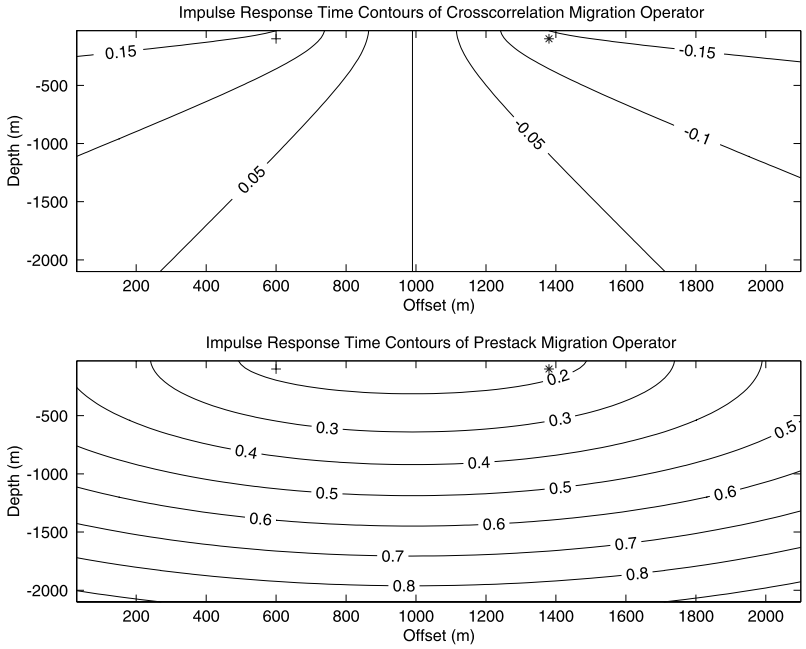

Figure 16. Isotime contours (in seconds) of the impulse response of the (top) cross-correlation migration and (bottom) pre-stack Kirchhoff migration operators. The + and * symbols represent the locations of the source and receiver, respectively, where the source location for the cross-correlograms is the same as the master trace. The cross-correlation migration operator is dominated by nearly vertical contours, so its resolution should be poorest in the vertical direction.

$2\cos\theta\omega/c\hat{\mathbf{i}}$, where θ is the angle of the ray with respect to the horizontal; the unit vector along the horizontal is denoted by $\hat{\mathbf{i}}$. There is no vertical wavenumber component so the vertical resolution of the scatterer buried midway between A and B is indeterminate from this pair of traces. This is seen in the Fig. 16 plot with the vertical contour line midway between the two trace positions.

5 CONCLUSIONS

A general methodology is presented for using correlated data to image source locations or reflector boundaries in $v(x, y, z)$ media. Traces are cross-correlated in time and weighted by the appropriate migration kernel, and summation over all geophone positions is carried out to give the migrated image (e.g. eq. 8). Our analysis supports Claerbout's conjecture: cross-correlating a trace at A with one at B yields a trace with the ghost–direct correlation kinematically equivalent to a primary reflection generated by a source at A and recorded at B. Both synthetic and field data examples are presented, which highlight both the efficacy and weaknesses of II. Further support of Claerbout's conjecture is provided by Wapenaar *et al.* (2002) and Wapenaar *et al.* (2003). However, II is not restricted to a random distribution of sources beneath the layers: it can be used for an arbitrary distribution of sources and can image both source locations and reflectivity from other events besides the ghost reflection.

A key merit of II is the potential to image the reflectivity distribution and source locations from passive seismic data when the source location and wavelets are not known. For multiple sources with overlapping time histories, the source wavelets must be uncorrelated for successful II. In the case of autocorrelation migration, defocusing of the image from static and migration-velocity errors can be significantly reduced by II.

The main disadvantage of II is the presence of virtual multiples in the correlated data, which can lead to severe migration artefacts. Therefore, coherent noise reduction should be applied to the correlated data prior to migration. For this reason, II will enjoy the most success with VSP data where many unwanted coherent events can be easily filtered out. Simultaneous use of the primary reflection and ghost reflection imaging conditions should also be used, as well as the joint imaging concept described in the text. Sometimes raw data can be time shifted to that of a direct or reflected arrival and then migrated according to an II condition (Sheley & Schuster 2003). This avoids the need to correlate data altogether. Otherwise, deconvolution of the correlated wavelets is recommended. Another problem with imaging ghost multiples is that the estimated reflectivity image can be a product of the reflection coefficients at several bounce points.

There are still many open questions about the practical uses for II in seismic imaging. One area to be addressed is the application of II to data associated with rough layer interfaces and randomly distributed scatterers, e.g. rough basalt layers sandwiched between sediments. In this case, statistical analysis should be used (e.g. Goodman 1985; Stover 1995) to characterize both the model and imaging formulae. Some useful insights to how II is used with random media data and time reversal acoustics are in Borcea *et al.* (2002, 2003).

ACKNOWLEDGMENTS

The authors offer many thanks to Jon Claerbout at Stanford for hosting GTS (in spring of 2000) for a four-month sabbatical, which provided fertile ground for this interferometric research. A four-month sabbatical at the University of Minnesota Institute of Applied Math was crucial for writing the final part of this paper. The authors also gratefully appreciate the help of Lew Katz and Fred Followill for initiating the earlier work on autocorrelation migration under a DOE contract. The authors thank Yi Luo for suggesting the concept of combining images by coherence weighting and very beneficial discussions about II. Finally, the authors appreciate the review by Kees Wapenaar and his helpful suggestions and insights. Part of this work is funded by an NSF grant related to earthquake imaging.

REFERENCES

Baskir, E. & Weller, C.E., 1975. Sourceless reflection seismic exploration, *Geophysics,* **40,** 158–159.

Berkhout, A.J. & Verschuur, D.J., 1998. Wave theory based multiple removal, an overview. In *Expanded Abstracts of the 1998 Technical Programme of the Society of Exploration Geophysicists with Biographies,* pp. 1503–1506, Society of Exploration Geophysicists, Tulsa, OK, USA.

Berkhout, A.J. & Verschuur, D.J., 2000. Internal multiple removal - boundary-related and layer-related approach. In: *62nd Mtg. Eur. Assn. Geosci. Eng., Session: L0056*.

Beylkin, G., 1985. Imaging of discontinuities in the inverse scattering problem by inversion of a causal generalized Radon transform, *J. Math. Phys.,* **26,** 99–108.

Bleistein, N., 1984. *Mathematical methods for wave phenomena*, Academic Press Inc. (Harcourt Brace Jovanovich Publishers), New York, USA.

Borcea, L., Tsogka, C., Papanicolaou, G. & Berryman, J., 2002. Imaging and time reversal in random media, *Inverse Problems,* **18,** 1247–1279

Borcea, L., Papanicolaou, G. & Tsogka, C., 2003. Theory and applications of time reversal and interferometric imaging, *Inverse Problems,* **19,** 5139–5164.

Bostock, M.G. & Rondenay, S., 1999. Migration of scattered teleseismic body waves, *Geophys. J. Int.,* **137,** 732–746.

Claerbout, J.F., 1968. Synthesis of a layered medium from its acoustic transmission response, *Geophysics,* **33,** 264–269.

Cole, S., 1995. Passive seismic and drill-bit experiments using 2-D arrays, *PhD thesis*, Stanford University, Palo Alto, USA.

Daneshvar, M.R., Clay, C.S. & Savage, M.K., 1995. Passive seismic imaging using microearthquakes, *Geophysics,* **60,** 1178–1186.

Duvall, T.L., Jefferies, S.M., Harvey, J.W. & Pomerantz, M.A., 1993. Time-distance helioseismology, *Nature,* **362,** 430–432.

Giles, P.M., Duvall, T.L. & Scherrer, P.H., 1997. A subsurface flow of material from the sun's equator to its poles, *Nature,* **390,** 52–54.

Goodman, J., 1985. *Statistical Optics*, Wiley Interscience Publications, New York, USA.

Jack, I. & Thomsen, L., 1999. Recent advances show the road ahead for the electric oil field very clearly. In *Expanded Abstracts of the 1999 Technical Programme of the Society of Exploration Geophysicists with Biographies,* pp. 1982–1983, Society of Exploration Geophysicists, Tulsa, OK, USA.

Katz, L., 1990. Inverse vertical seismic profiling while drilling, *United States Patent*, Patent Number: 5,012,453.

Kosovichev, A.G., 1999. *Inversion methods in helioseismology and solar tomography*, submitted to Elsevier Preprint.

Langston, C.A., 1977. Corvallis, Oregon, crustal and upper mantle receiver structure from teleseismic P and S waves, *Bull. seism. Soc. Am.,* **67,** 713–724.

Loeb, D.T. & Pechmann, J.C., 1986. The P-wave velocity structure of the crust-mantle boundary beneath Utah from network travel time measurements, *Earthquake Notes,* **57,** 10.

Maxwell, S.C., Bossu, R., Young, R.P. & Dangerfield, J., 1998. Processing of induced microseismicity recorded in the Ekofisk reservoir. In *Expanded Abstracts of the 1998 Technical Programme of the Society of Exploration Geophysicists with Biographies*, pp. 1503–1506, Society of Exploration Geophysicists, Tulsa, OK, USA.

Rickett, J., 1996. The effects of lateral velocity variations and ambient noise source location on seismic imaging by cross-correlation, *Stanford Exploration Project,* **93,** 137–150.

Rickett, J. & Claerbout, J., 1996. Passive seismic imaging applied to synthetic data, *Stanford Exploration Project,* **92,** 83–90.

Rickett, J. & Claerbout, J., 1999. Acoustic daylight imaging via spectral factorization: Helioseismology and reservoir monitoring, *The Leading Edge,* **18,** 957–960.

Rickett, J.E. & Claerbout, J.F., 2000. Calculation of the acoustic solar impulse response by multi-dimensional spectral factorization, *Solar Physics,* **192**(1/2), 203–210.

Scherrer, P.H. *et al.*. the MDI Engineering Team, 1995. The Solar Oscillations Investigation - Michelson Doppler Imager, *Solar Physics,* **162**(1/2), 129–188.

Schuster, 2001. Seismic interferometry: Tutorial. In: 63rd Mtg. Eur. Assn. Geosci. Eng.

Schuster, G. T., 1999. Seismic interferometric imaging with waveforms, *Utah Tomography and Modeling-Migration Project Midyear Report*, 121–130.

Schuster, G. & Rickett, J., 2000. Daylight imaging in V(x, y, z) media, *Utah Tomography and Modeling-Migration Project Midyear Report and Stanford Exploration Project Midyear Reports*, pp. 55–66.

Schuster, G., Followill, F., Katz, L., Yu, J. & Liu, Z., 2003. Autocorrelogram migration: Theory, *Geophysics*, **68,** 1685–1694.

Schuster, G.T., Liu, Z. & Followill, F., 1997. Migration of autocorrelograms. In *Expanded Abstracts of the 1997 Technical Programme of the Society of Exploration Geophysicists with Biographies*, pp. 1893–1896, Society of Exploration Geophysicists, Tulsa, OK, USA.

Shapiro, S.A., Audigane, P. & Royer, J., 1999. Large-scale in situ permeability tensor of rocks from induced microseismicity, *Geophys. J. Int.,* **137,** 207–213.

Sheley, D. & Schuster, G.T., 2003. Reduced time migration of transmission PS waves, *Geophysics,* **68,** 1695–1707.

Sheng, J., 2001. Migration of multiples and primaries in CDP data by cross-correlogram migration. In *Expanded Abstracts of the 2001 Technical Programme of the Society of Exploration Geophysicists with Biographies*, pp. 1297–1300, Society of Exploration Geophysicists, Tulsa, OK, USA.

Sheng, J., Schuster, G.T. & Nowack, R., 2001. Imaging of crustal layers by teleseismic ghosts, *EOS, Trans. Am. geophys. Un.,* **82**, Abstract S32C–0658.

Snieder, R., Gret, A., Douma, H. & Scales, J., 2002. Coda wave interferometry for estimating nonlinear behavior in seismic velocity, *Science,* **295,** 2253–2255.

Stover, J., 1995. *Optical Scattering: Measurement and Analysis*, SPIE Optical Engineering Press.

Sun, H. & Schuster, G.T., 2001. 2-D wavepath migration, *Geophysics,* **66,** 1528–1537.

Wapenaar, K., Dragonov, D. & Fokkema, J., 2002. Codas in reflection and transmission responses and their mutual relations. In: *64th Ann. Int. Mtg. of EAGE (Expanded Abstracts)*.

Wapenaar, K., Dragonov, D. & Fokkema, J., 2003. Synthesis of an inhomogeneous medium from its acoustic transmission response, *Geophysics,* **68,** 1756–1559.

Yu, J., Katz, L., Followill, F. & Schuster, G., 2003. Autocorrelogram migration of IVSPWD data: Field data test, *Geophysics,* **68,** 297–307.

APPENDIX A: STATIONARY PHASE APPROXIMATION

To mathematically justify, in a stationary-phase sense, the migration of free-surface reflections with eq. (8), we focus attention on the correlation $\tilde{\Phi}(A, B)_{\mathrm{dir}_A-\mathrm{gh}_B}$ in eq. (6), except we do not assume that the dominant contribution is a specular reflection at A. Instead, the $\tilde{\Phi}(A, B)_{\mathrm{dir}_A-\mathrm{gh}_B}$ correlation is given by an integral over the scattering points A' on the free surface

$$\tilde{\Phi}(A, B)_{\mathrm{dir}_A-\mathrm{gh}_B} = -Re^{-i\omega\tau_{sA}} \int_{-\infty}^{\infty} e^{i\omega(\tau_{sA'}+\tau_{A'x}+\tau_{Bx})}\, dA', \qquad \text{(A1)}$$

where geometrical spreading is ignored and x is the location of the scatterer.

Applying the stationary-phase approximation at high frequencies to the above integral yields

$$\tilde{\Phi}(A, B)_{\mathrm{dir}_A-\mathrm{gh}_B} \sim -CRe^{-i\omega\tau_{sA}} e^{i\omega(\tau_{sA_{\mathrm{spec}}}+\tau_{A_{\mathrm{spec}}x}+\tau_{Bx})}, \qquad \text{(A2)}$$

where C is an asymptotic coefficient term (Bleistein 1984) and the location A_{spec} is the stationary value that satisfies the following equation:

$$\partial\tau_{sA}/\partial A = -\partial\tau_{Ax}/\partial A. \qquad \text{(A3)}$$

This equation is satisfied when $A = A_{\mathrm{spec}}$ is the specular reflection point on the free surface as shown by the ray path *sA* in Fig. 2(a):

i.e. the angle of the upcoming source ray sA is equal and opposite to the reflection ray Ax at the specular reflection point A_{spec} on the free surface.

Applying the ghost migration kernel $e^{-i\omega(\tau_{Ax'}+\tau_{Bx'})}$ in eq. (7) to $\tilde{\Phi}(A, B)_{\text{dir}_A-\text{gh}_B}$ in eq. (A2) and integrating over all A yields the migration image

$$m(x') = -CR \int e^{i\omega(-\tau_{sA}+\tau_{sA_{spec}}+\tau_{A_{\text{spec}}x}+\tau_{Bx})} \times e^{-i\omega(\tau_{Ax'}+\tau_{Bx'})}\, dA, \tag{A4}$$

which asymptotically becomes

$$\sim -CC'Re^{i\omega(-\tau_{sA^*}+\tau_{sA_{\text{spec}}}+\tau_{A_{\text{spec}}x}+\tau_{Bx}-\tau_{A^*x'}-\tau_{Bx'})}, \tag{A5}$$

where A^* is the new stationary phase point and C' is its associated asymptotic coefficient term. In this case, the stationary phase condition is

$$\partial\tau_{sA}/\partial A|_{A^*} = -\partial\tau_{A^*x'}/\partial A|_{A^*}, \tag{A6}$$

which is the same as the previous one when the trial image point x' coincides with the scatterer location x, so that $A^* = A_{\text{spec}}$. In this case, the exponent in eq. (A5) goes to zero as $A^* \to A_{\text{spec}}$ and $x' \to x$, so that summation over all frequencies and values of B leads to constructive interference of the migrated free-surface reflections at the scatterer location. Conversely, if the image point x' is not coincident with x then there will be mostly destructive superposition of migrated free-surface reflections away from the actual scatterer location.

Note that the migration operator does not depend on the source position or the scatterer location or depth, so this procedure also applies to data generated by a random distribution of sources and a medium with many scatterers. It is straightforward to append a summation over scatterers to generalize this procedure to arbitrary reflector boundaries.